# Supporting Information

# A Silver-chalcogenide Nanomaterial Enveloped with a Carborane-thiolate Shell for the Electroreduction of $CO_2$ to CO

*Arijit Jana*[1], *Zhengyuan Li*[2], *Amoghavarsha Ramachandra Kini*[1], *Vivek Yadav*[1], *Akhil S. Nair*[3], *Astrid Campos Mata*[4], *Jingjie Wu*[2], *Jan Macháček*[5], *Tomas Base*[5*], *Biswarup Pathak*[3*], *Soumyabrata Roy*[4,6*], *Thalappil Pradeep*[1*]

[1]DST Unit of Nanoscience (DST UNS) and Thematic Unit of Excellence (TUE), Department of Chemistry, Indian Institute of Technology, Madras, Chennai – 600036, India

[2]Department of Chemical and Environmental Engineering, University of Cincinnati, Cincinnati, OH 45221, USA

[3]Department of Chemistry, Indian Institute of Technology Indore, Indore 453552, India

[4]Department of Materials Science and Nanoengineering, Rice University, Houston, TX 77005 USA

[5]Department of Syntheses, Institute of Inorganic Chemistry, The Czech Academy of Science, 1001 Husinec-Rez, 25068, Czech Republic

[6]Department of Sustainable Energy Engineering, Indian Institute of Technology Kanpur, Kanpur, Uttar Pradesh 208016, India

Email: pradeep@iitm.ac.in, soumyar@iitk.ac.in, biswarup@iiti.ac.in, tbase@iic.cas.cz

**Table of Content:**

# Experimental section

## Chemicals used

Silver nitrate ($AgNO_3$) was purchased from Rankem Chemicals. The $M_9$-COOH ligand was synthesized following our earlier report, using *meta*-carborane 9-thiol derivative.[1] Solvent grade dichloromethane, dimethylformamide, and methanol were purchased from Rankem chemicals and Finar, India. All chemicals were used as such without further purification.

## Synthesis of Ag-CBT framework solid

The Ag-CBT framework was synthesized using a modified solvothermal method. Initially, 25 mg (24.52 mM) of $AgNO_3$ was dissolved in 1.5 ml of methanol under ultrasonic conditions. Then, 35 mg of $M_9$-COOH (26.51 mM) was added after being dissolved in 4.5 ml of DMF. A few drops of trimethylamine were introduced to the mixture. After stirring for one hour, the resulting transparent solution was transferred to a hydrothermal container with a Teflon-lined inner chamber. The mixture underwent hydrothermal treatment at 80 °C for 48 hours. After this period, it was allowed to cool slowly to room temperature. Colorless rod-shaped crystals were observed at the bottom of the Teflon cylinder and were collected through centrifugation. These crystals were washed with methanol (3 × 5 ml) and subsequently used for further studies. The yield of the Ag-CBT framework was determined to be 85 % based on the amount of silver precursor used.

To investigate the effect of temperature during the solvothermal synthesis, we conducted experiments across a range of temperatures from 60 °C to 150 °C. At 60 °C, no crystalline solids were formed after 48 hours of heating. Reactions conducted between 80 °C and 120 °C produced white microcrystalline solids, while reactions at 150 °C resulted in black precipitates. Comparative powder X-ray diffraction analysis showed that maintaining temperatures between 80 °C and 100 °C for 48 to 72 hours led to the formation of phase-pure Ag-CBT solids (shown in Figure S17).

## Preparation of gas diffusion electrode

Sample-loaded catalyst inks were prepared using the air-brush method. First, microcrystalline powder of Ag-CBT solid was dispersed in isopropanol containing 5 wt% Nafion solution and the mixture was sonicated for 20 min. Afterward, the catalyst ink was air-brushed onto a gas diffusion layer (GDL, Sigracet 35BC, Fuel Cell Store) to create a gas diffusion electrode (GDE). The prepared GDE was dried at 80 °C under vacuum for 30 min. The catalyst loading for cathode electrodes was kept at ≈ 0.5 mg cm$^{-2}$. The loading was calculated by weighing the GDL before and after coating catalyst layer.

## Electrochemical $CO_2$ reduction measurements

A specially designed flow cell was used to evaluate $CO_2$ electroreduction under ambient conditions. In this setup, a catalyst-loaded gas diffusion electrode (GDE) served as the cathode, while nickel foam was used as the anode, with a 1 M KOH solution as the electrolyte. An FAA-3-PK-75 anion exchange membrane (from Fuel Cell Store) separated the cathodic and anodic compartments. The electrolyte was delivered using syringe pumps (New Era Pump Systems Inc.) at flow rates of 1.5 mL/min to the cathode and 2.0 mL/min to the anode. A $CO_2$ gas flow of 50 sccm was maintained at the cathode using an Alicat Scientific mass flow controller. A Gamry Interface 1010E potentiostat was employed to apply a constant voltage to the flow cell and measure the resulting current from the catalyst. The cathode potential was continuously monitored relative to an Ag/AgCl (3 M KCl) reference electrode by a multimeter (Fluke Store). The potentials were adjusted to the RHE scale using the following equation: $E_{RHE} = E_{Ag/AgCl} + 0.209\ V + 0.0591 \times pH$. Because of rapid dynamic evolutions of local environments,[2] the resistance (R) between the cathode and reference electrode was immediately measured using potentiostatic electrochemical impedance spectroscopy (EIS) after each electrolysis, and then the ohmic drop (iR) was manually compensated. The R was measured to be 3.1-3.3 Ω.

## Product analysis

An online gas chromatograph (GC, SRI Instruments Multiple Gas) equipped with a flame ionization detector (FID) and a thermal conductivity detector (TCD) was used to analyze the gas products at each applied potential. The Faradaic efficiency (FE) for gas products was calculated using: $FE\ (\%) = zFxV \times 100\% / j_{total}$, where $j_{total}$ is total current density; V is molar flow rate of outlet $CO_2$; x is the molar fraction of product with respect to $CO_2$ as determined by GC; F is Faraday constant; z is the number of electrons involved to form the target product. Argon gas was supplied at a rate of 10 sccm to the outlet gas stream of the flow cell before it was directed to the GC, enabling accurate determination of the actual $CO_2$ flow rate after electrolysis. Standard deviations were calculated from measurements taken on three separate electrodes.

# Instrumentation

## Optical microscopy

Optical microscopic images of crystals were collected in transmission mode using a LEICA optical microscope equipped with LAS V4.8 software. The polarization of the crystal was measured using an optical polarizer.

## Scanning electron microscopy (SEM)

Scanning electron microscopic images are measured using a Verios G4 UC, Thermo Scientific field emission scanning electron microscope (FESEM). After transferring the sample on a carbon tape, gold sputtering was performed to increase the conductivity of the sample. All the images were collected in high vacuum at an operating voltage of 10-15 kV. Energy dispersive analysis of X-ray (EDAX) was performed using the same instrument.

## Scanning transmission electron microscopy (STEM)

Morphology characterization and single atom imaging of the framework was performed using FEI Titan Themis3 STEM equipped with a field emission gun operating at 200kV. For STEM observations, a suspension of the sample in ethanol was sonicated for 15 min and then drop-casted to a Cu grid with a lacey carbon support and dried for 5 min. The “beam shower” procedure was performed for 30 mins to reduce hydrocarbon contamination during subsequent imaging at high magnification.

## UV-vis absorption spectroscopy

The UV-vis absorption spectrum was measured at room temperature in reflectance mode using an Agilent Cary 5000 UV-Vis-NIR spectrophotometer equipped with a 6-inch integrating sphere. The microcrystalline samples were dispersed in NVH immersion oil, crushed between two quartz plates, and the resulting thin layer was used for measurement.

## Mass spectrometry

The mass spectrum of Ag-CBT framework solid was measured using Waters Synapt G2Si HDMS instrument. The instrument was equipped with an electrospray ionization source, step wave ion transfer optics, a quadrupole mass filter, and time of flight detector. Each mass spectrum was recorded both in positive and negative ion-modes. An optimized condition of flow rate 25-30 µl/min, capillary voltage 2.5-3 kV, cone voltage 0 kV, spray current 100-125 nA, source temperature 70-100 °C and desolation temperature 90-120 °C with gas flow rate of 300 L/h were used for the measurements.

### Infrared spectroscopy

Perkin Elmer Fourier Transform Infrared spectrometer (FT-IR) was used to measure the vibrational spectra of the Ag-CBT framework. Thin pallet was made by compressing a fine mixture of dry KBr with a small amount of microcrystalline sample.

### Raman spectroscopy

Raman spectra were recorded using a CRM-Alpha 300S, WI Tec GmbH confocal Raman microscope, equipped with 532 nm frequency doubled Nd:YAG laser and 632 nm Helium Neon laser. Laser beam was focused to the sample using an objective lense having 20x magnification. The dispersed light from the sample was collected by a Peltier cooled CCD detector.

### Powder X-ray diffraction

Powder XRD measurements were performed using a Bruker D8 Advance instrument equipped with a Cu Kα X-Ray source (hν = 8047.8 eV). The microcrystalline sample was prepared as a thin layer on a glass slide for the measurements.

### Thermogravimetric analysis

Thermogravimetric measurements in the temperature range of 25 to 800 °C were performed using a NETZSCH STA 449 F3 Jupiter instrument equipped with Proteus-6.1.0 software. Around 1.5 mg of crystalline sample was loaded into an alumina crucible for the measurement. Nitrogen and argon were used as purge gases during the measurement with a thermal flow rate of 10 °C/min.

### Crystallographic details

Single crystal X-ray diffraction (SC-XRD) of a good quality single crystal was performed using a Bruker D8 VENTURE single crystal X-ray diffractometer equipped with graphite monochromatic Mo Kα ($\lambda$ = 0.71073 Å) radiation and a PHOTON 100 CMOS detector. The data collection was performed at 283 K. The automatic cell determination routine, with 24 frames at two different orientations of the detector was employed to collect reflections for unit cell determination. Further, intensity dates for structure determination were collected through an optimized strategy which gave an average 4-fold redundancy. The program APEX3-SAINT (Bruker, 2016) was used for integrating the frames, followed by a multi-scan absorption correction using the program SADABS

(Bruker, 2016). The structure was solved by SHELXT-2014 (Sheldrick, 2014) and refined by full-matrix least squares techniques using SHELXL-2018, (Sheldrick, 2018) software package. Hydrogens on all carbon and boron atoms were fixed at calculated positions and refined as riding model with C-H or B-H = 1.10 Å, $U_{iso}(H) = 1.2U_{eq}$ (C or B).

## Computational details

The DFT calculations are carried out using Vienna Ab-Initio Simulation Package (VASP) with generalized gradient approximation (GGA) of Perdew–Burke–Ernzerhof (PBE) functional.[3,4] Projector augmented wave (PAW) method is used for treating ion electron interactions.[5] The ionic relaxations have been carried out using a conjugate gradient algorithm with convergence criteria of $10^{-4}$ eV for minimum energy and 0.05 eVÅ$^{-1}$ for Hellmann-Feynman forces on atoms. The Brillouin zone was sampled at the Gamma point (1×1×1). To study the energetics of $CO_2$ electrochemical reduction, we have used computational hydrogen electrode (CHE) model.[6]

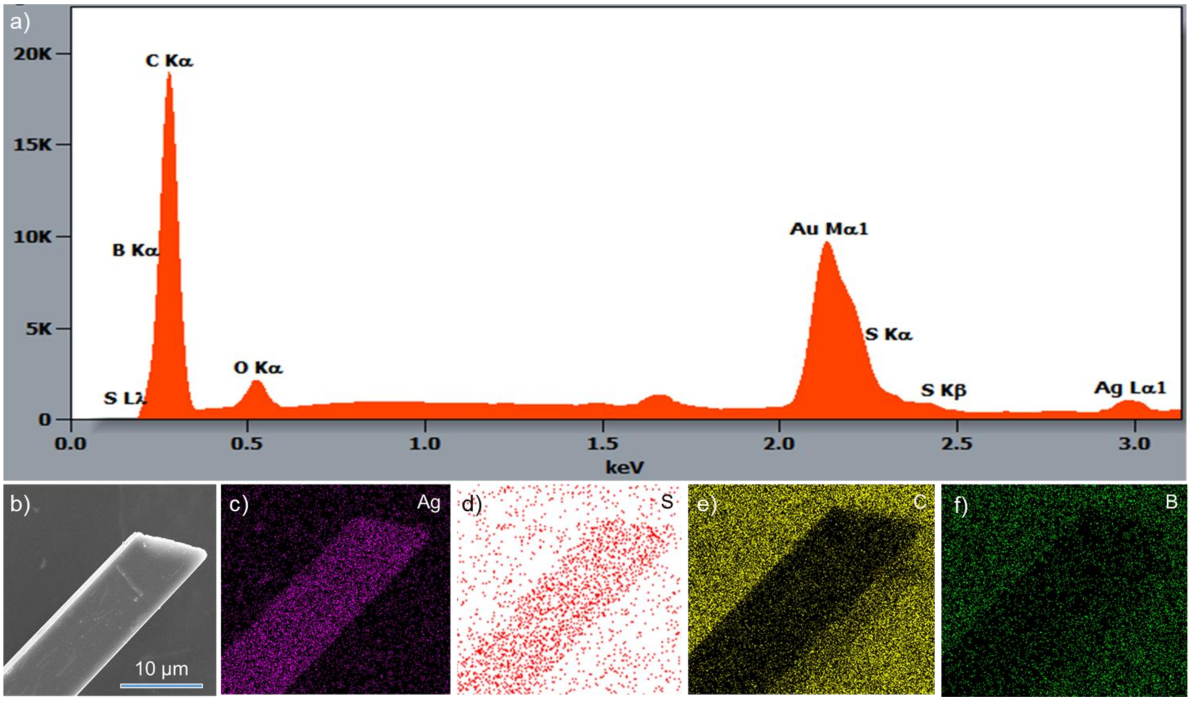

**Figure S1.** a) The EDS spectral profile of Ag-CBT crystal. b) FESEM micrograph of a single crystal used for elemental mapping. c-f) Elemental maps of the respective elements present in the crystal. The Au content is due to the gold sputtering on the crystal.

**Table S1.** Crystal data and structure refinement for Ag-CBT framework.

| | | |
|---|---|---|
| Identification code | Ag-CBT | |
| CCDC | 2431392 | |
| Empirical formula | $C_2H_{11}AgB_{10}S$ | |
| Formula weight | 283.14 | |
| Temperature | 200(2) K | |
| Wavelength | 0.71073 Å | |
| Crystal system | Monoclinic | |
| Space group | P 21/m | |
| Unit cell dimensions | a = 9.2333(15) Å | α= 90°. |
| | b = 7.1911(10) Å | β= 97.372(6)°. |
| | c = 15.961(3) Å | γ = 90°. |
| Volume | 1051.0(3) $Å^3$ | |
| Z | 4 | |
| Density (calculated) | 1.789 $Mg/m^3$ | |
| Absorption coefficient | 2.051 $mm^{-1}$ | |
| F(000) | 544 | |
| Crystal size | 0.200 x 0.150 x 0.100 $mm^3$ | |
| Theta range for data collection | 2.709 to 30.047°. | |
| Index ranges | -12<=h<=12, -10<=k<=10, -22<=l<=22 | |
| Reflections collected | 35235 | |
| Independent reflections | 3262 [R(int) = 0.0471] | |
| Completeness to theta = 25.242° | 99.5 % | |
| Absorption correction | Semi-empirical from equivalents | |
| Max. and min. transmission | 0.7460 and 0.6476 | |
| Refinement method | Full-matrix least-squares on $F^2$ | |
| Data / restraints / parameters | 3262 / 64 / 148 | |
| Goodness-of-fit on $F^2$ | 1.054 | |
| Final R indices [I>2sigma(I)] | R1 = 0.0422, wR2 = 0.0897 | |
| R indices (all data) | R1 = 0.0485, wR2 = 0.0935 | |
| Extinction coefficient | n/a | |
| Largest diff. peak and hole | 1.895 and -1.645 $e.Å^{-3}$ | |

**Table S2.** Atomic coordinates ($\times 10^4$) and equivalent isotropic displacement parameters ($Å^2 \times 10^3$) for Ag-CBT framework. U(eq) is defined as one third of the trace of the orthogonalized $U^{ij}$ tensor.

| | x | y | z | U(eq) |
|---|---|---|---|---|
| Ag(1) | 3697(1) | 4816(1) | 8912(1) | 35(1) |
| S(1) | 2091(1) | 2500 | 8211(1) | 21(1) |
| S(2) | 5041(1) | 7500 | 9469(1) | 22(1) |
| B(1) | 2491(5) | 2500 | 7094(3) | 21(1) |
| B(2) | 1416(8) | 3704(13) | 6268(3) | 80(3) |
| B(3) | 1562(9) | 2500 | 5366(4) | 61(2) |
| B(4) | 3255(8) | 2500 | 5068(4) | 39(1) |
| B(5) | 4219(8) | 3665(11) | 5874(3) | 74(2) |
| B(6) | 4270(8) | 2500 | 6823(4) | 67(3) |
| B(7) | 3175(11) | 545(8) | 6613(3) | 76(2) |
| B(8) | 6691(5) | 7500 | 8903(3) | 19(1) |
| B(9) | 6660(8) | 7500 | 7786(4) | 70(3) |
| B(10) | 7286(6) | 9447(8) | 8379(5) | 65(2) |
| B(11) | 8203(6) | 8711(14) | 7529(4) | 88(3) |
| B(12) | 9773(7) | 7500 | 7948(4) | 38(1) |
| B(13) | 9832(7) | 7500 | 9055(5) | 50(2) |
| B(14) | 8296(5) | 8701(10) | 9313(4) | 58(2) |
| C(1) | 2531(12) | 4420(9) | 5523(4) | 98(2) |
| C(2) | 9138(5) | 9265(7) | 8462(4) | 60(1) |

**Table S3.** Anisotropic displacement parameters (Å$^2$×10$^3$) for Ag-CBT framework. The anisotropic displacement factor exponent takes the form: -2p$^2$[ h$^2$a*$^2$U$^{11}$ + ... + 2 h k a* b* U$^{12}$ ]

| | $U^{11}$ | $U^{22}$ | $U^{33}$ | $U^{23}$ | $U^{13}$ | $U^{12}$ |
|---|---|---|---|---|---|---|
| Ag(1) | 28(1) | 41(1) | 36(1) | -15(1) | 11(1) | -13(1) |
| S(1) | 19(1) | 23(1) | 20(1) | 0 | 4(1) | 0 |
| S(2) | 21(1) | 22(1) | 23(1) | 0 | 3(1) | 0 |
| B(1) | 19(2) | 22(2) | 20(2) | 0 | 1(2) | 0 |
| B(2) | 82(4) | 135(7) | 24(2) | 16(3) | 6(2) | 77(5) |
| B(3) | 35(3) | 128(8) | 17(3) | 0 | -4(2) | 0 |
| B(4) | 46(4) | 49(4) | 21(3) | 0 | 3(2) | 0 |
| B(5) | 101(4) | 101(5) | 21(2) | -6(3) | 15(2) | -74(4) |
| B(6) | 24(3) | 158(9) | 21(3) | 0 | 4(2) | 0 |
| B(7) | 174(8) | 29(3) | 30(2) | 4(2) | 35(4) | 35(3) |
| B(8) | 19(2) | 18(2) | 19(2) | 0 | -1(2) | 0 |
| B(9) | 22(3) | 166(9) | 21(3) | 0 | -1(2) | 0 |
| B(10) | 43(3) | 35(3) | 126(5) | 46(3) | 43(3) | 17(2) |
| B(11) | 39(3) | 165(8) | 63(3) | 73(4) | 21(2) | 23(4) |
| B(12) | 28(3) | 52(4) | 36(3) | 0 | 12(2) | 0 |
| B(13) | 20(3) | 95(6) | 33(3) | 0 | -2(2) | 0 |
| B(14) | 26(2) | 90(4) | 60(3) | -53(3) | 14(2) | -25(2) |
| C(1) | 209(7) | 54(3) | 38(3) | 19(3) | 37(4) | 40(4) |
| C(2) | 41(2) | 27(2) | 119(4) | -3(2) | 42(3) | -10(2) |

**Table S4.** Hydrogen coordinates (×$10^4$) and isotropic displacement parameters (Å$^2$×$10^3$) for Ag-CBT framework.

| | x | y | z | U(eq) |
|---|---|---|---|---|
| H(2) | 431 | 4518 | 6390 | 96 |
| H(3) | 609 | 2500 | 4856 | 73 |
| H(4) | 3533 | 2500 | 4405 | 46 |
| H(5) | 5191 | 4495 | 5741 | 88 |
| H(6) | 5245 | 2500 | 7319 | 81 |
| H(7) | 3398 | -783 | 6973 | 91 |
| H(9) | 5602 | 7500 | 7355 | 84 |
| H(10) | 6659 | 10783 | 8351 | 78 |
| H(11) | 8176 | 9552 | 6936 | 106 |
| H(12) | 10793 | 7500 | 7637 | 46 |
| H(13) | 10896 | 7500 | 9480 | 60 |
| H(14) | 8346 | 9538 | 9908 | 70 |
| H(1) | 2180(60) | 5480(60) | 5150(30) | 72 |
| H(2C) | 9610(60) | 10390(50) | 8340(40) | 72 |

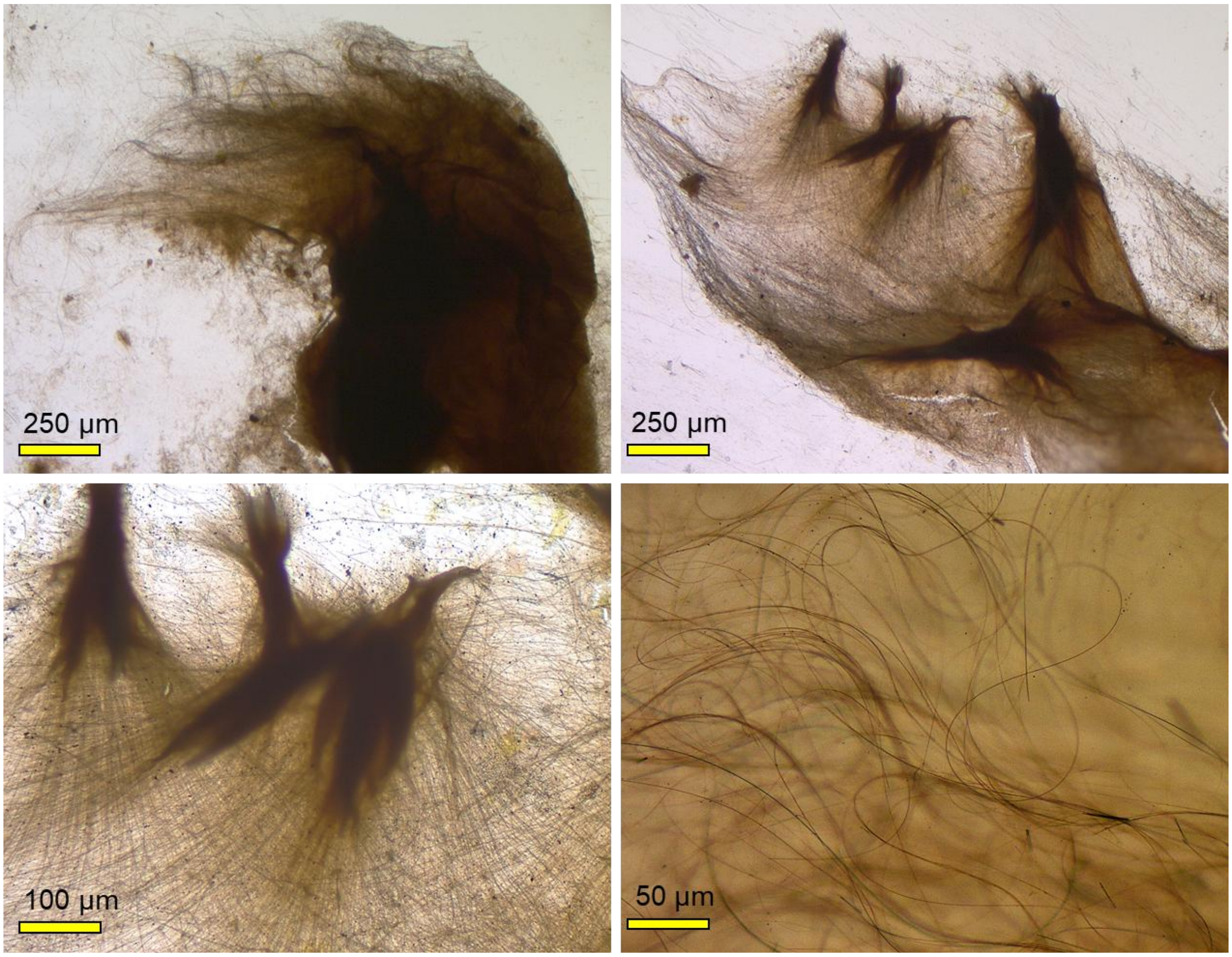

**Figure S2.** Optical micrographs of the hair-like solids formed from the hydrothermal reaction of $AgNO_3$ and $M_9$ ligand, captured at varying magnifications.

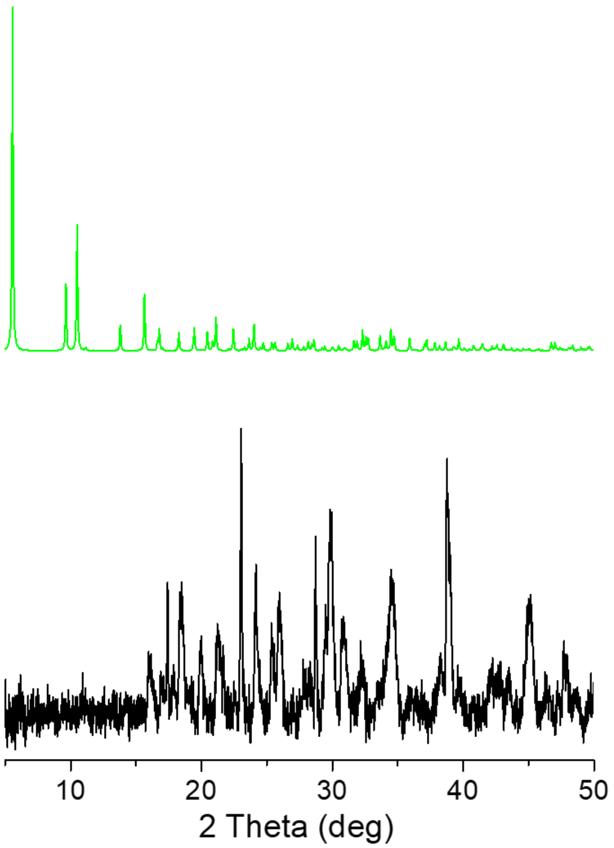

**Figure S3.** Powder X-ray diffraction pattern of the hair like solids (black trace) obtained after the 48 hours hydrothermal reaction of $AgNO_3$ and $M_9$ ligand. A comparative simulated diffraction pattern (green trace) of Ag-CBT is also shown here.

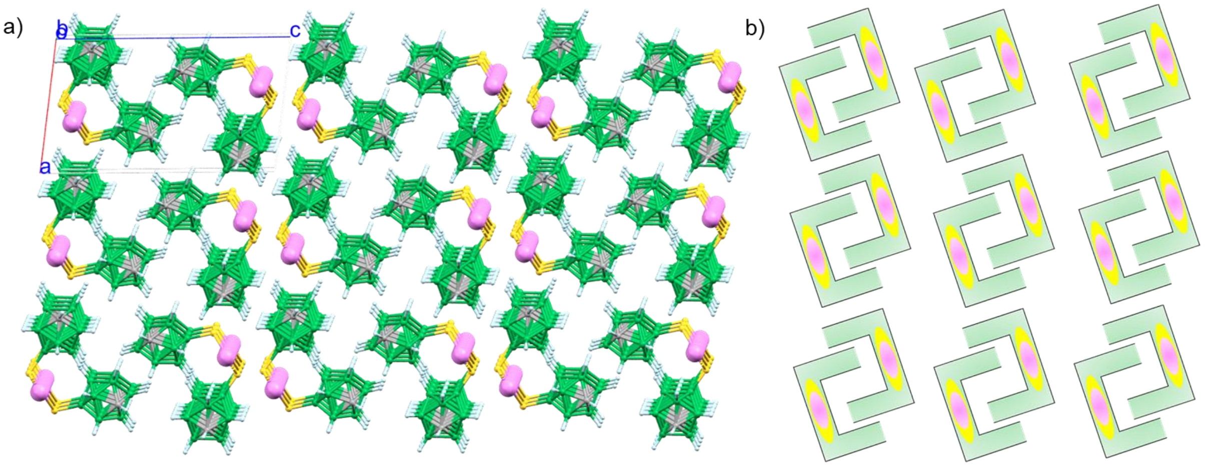

**Figure S4.** a) The (3×3×3) extended packing of the Ag-CBT framework reveals two one-dimensional U-shaped interlocking layers. Color code: pink =Ag, yellow = S, green = B, grey = C, light blue = H. b) Schematic representation of the interlocking.

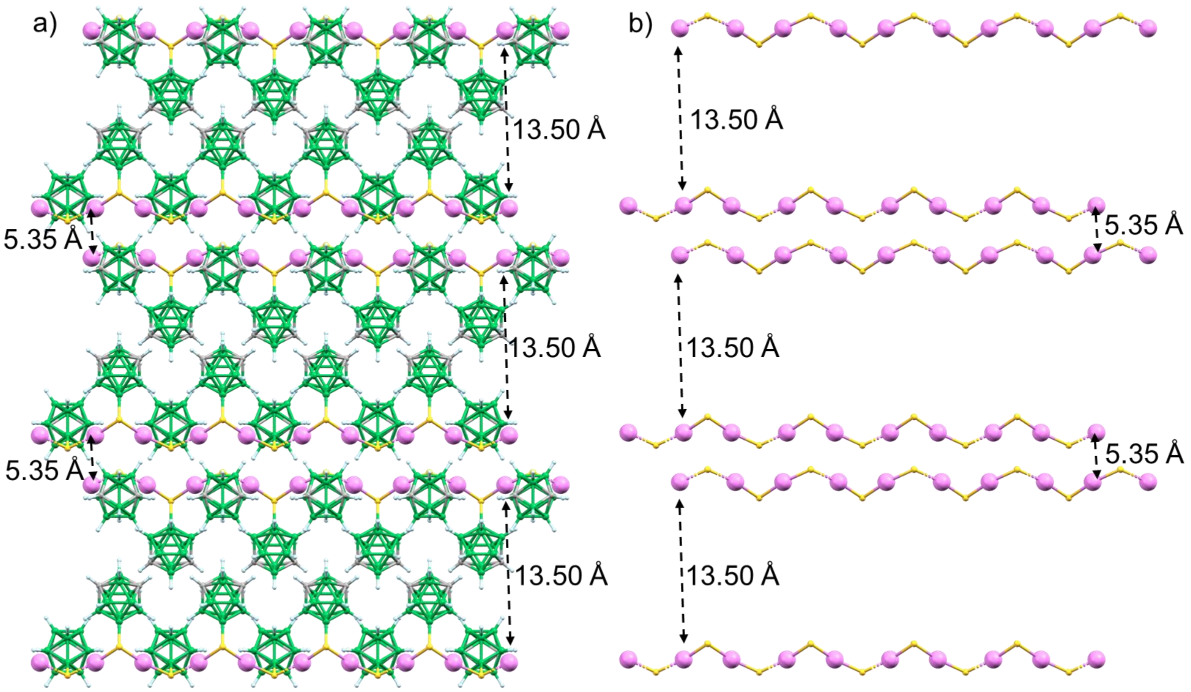

**Figure S5.** a) An extended packing structure of the Ag-CBT solid along the a-axis, featuring notable Ag···Ag distances. b) The same framework without carboranes.

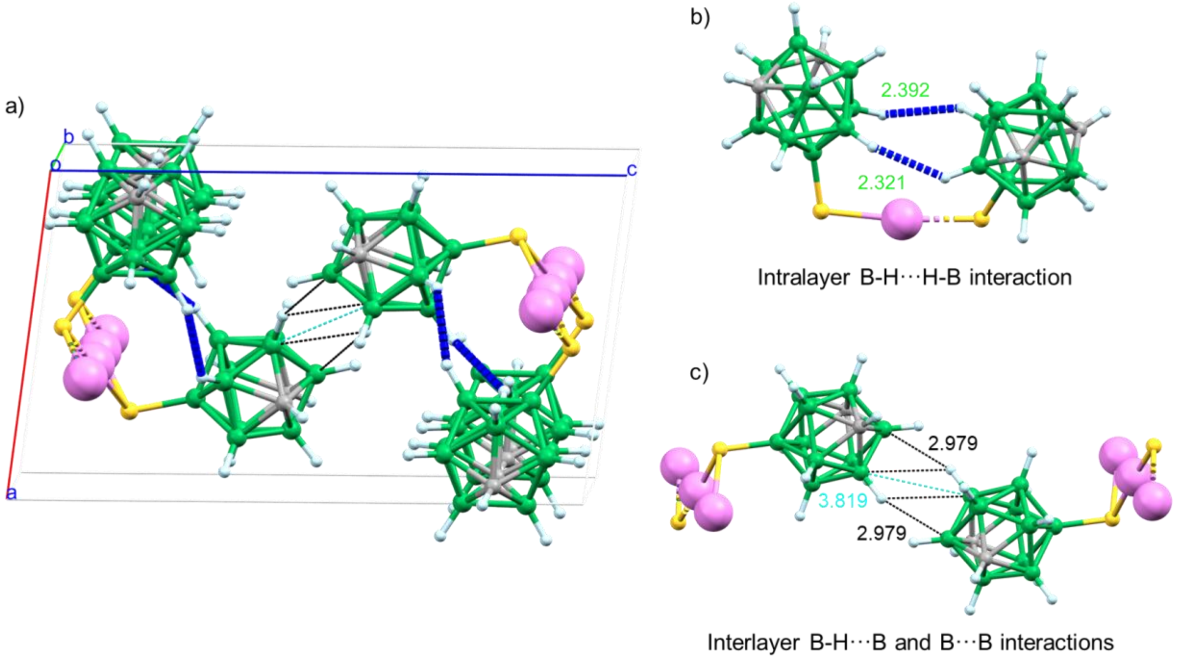

**Figure S6.** a) Carborane-centered short-contact intermolecular interactions were observed between the two layers. Expanded view of b) intralayer B-H···H-B interactions, and c) interlayer B-H···B and B···B interactions.

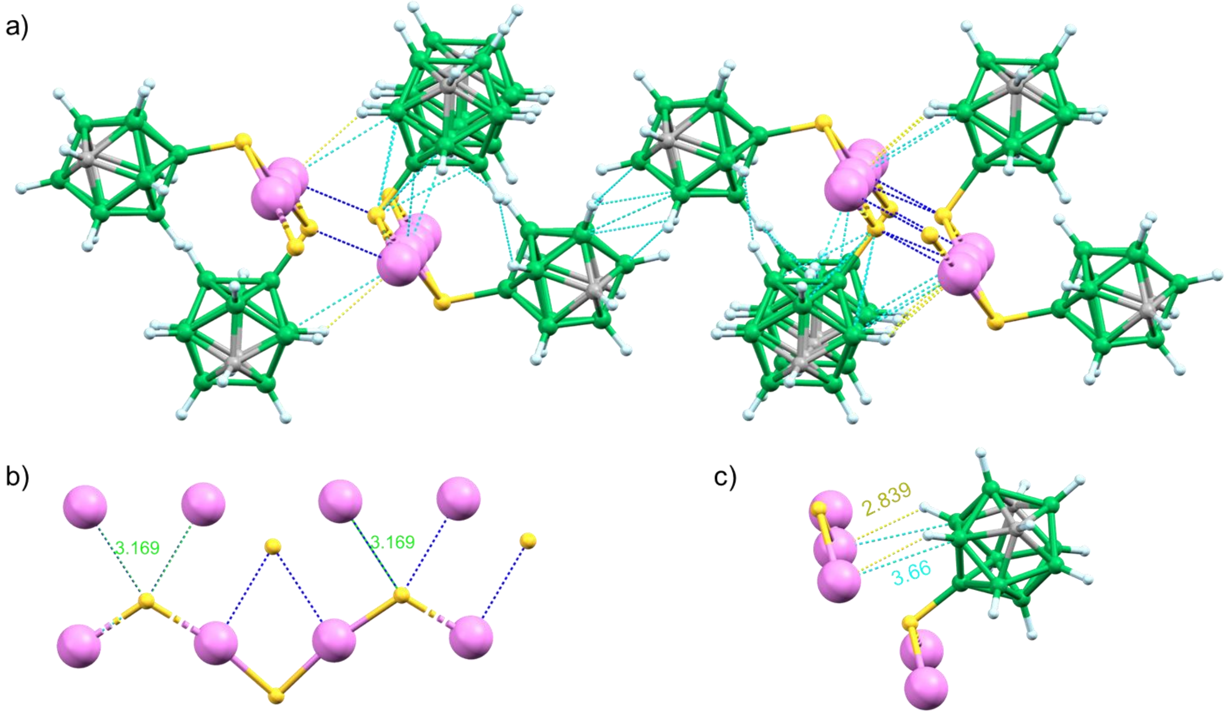

Ag···S interactions

Ag···H-B and Ag···B interactions

**Figure S7.** a) Metal-centered short contact intermolecular interactions observed in Ag-CBT framework solids. Expanded view of b) Ag···S interactions, and c) B-H···Ag and Ag···B interactions.

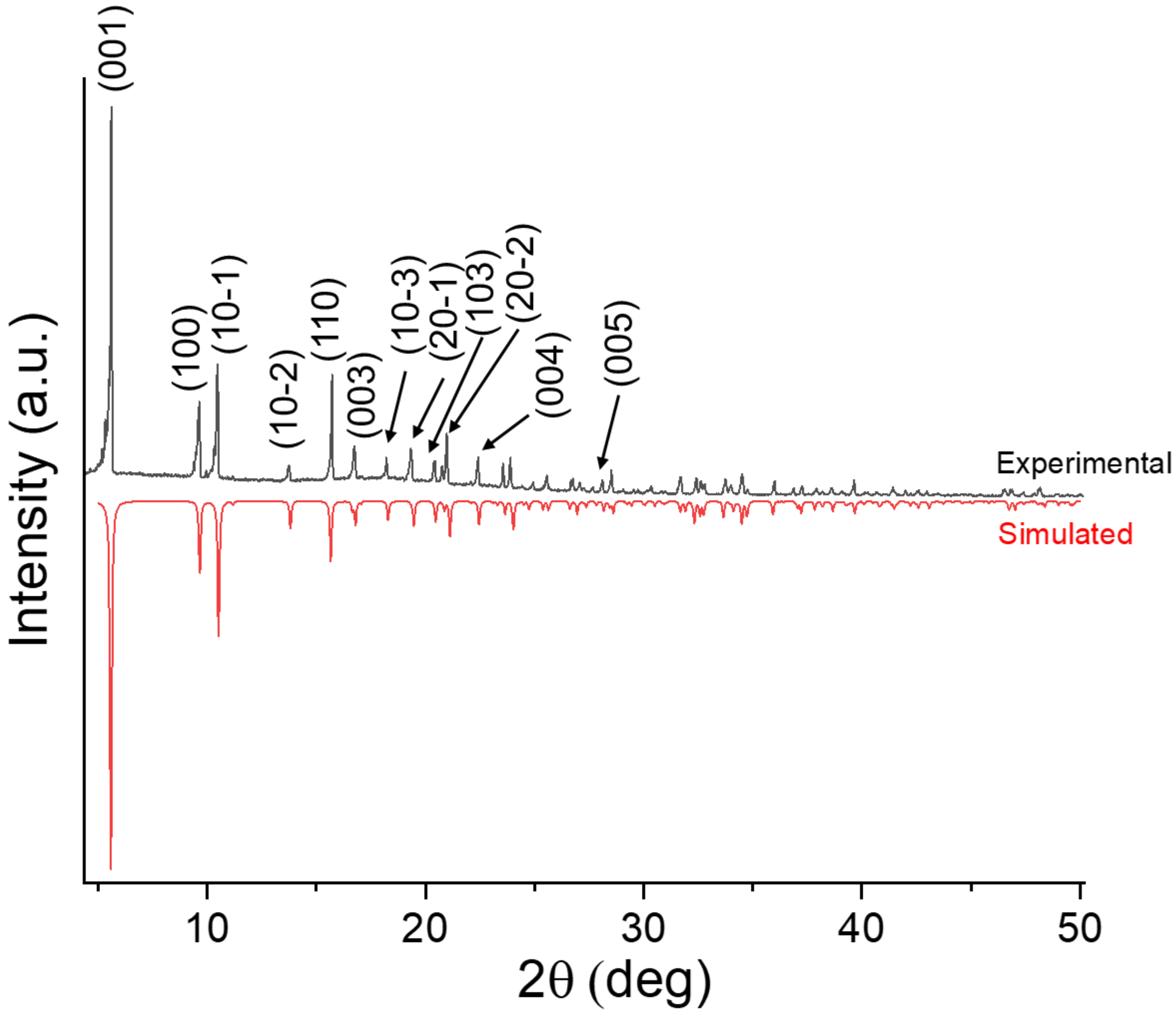

**Figure S8.** The experimental PXRD spectrum of the Ag-CBT framework compared with the simulated spectrum obtained from SCXRD data. Peaks of interest in the lower region are assigned here.

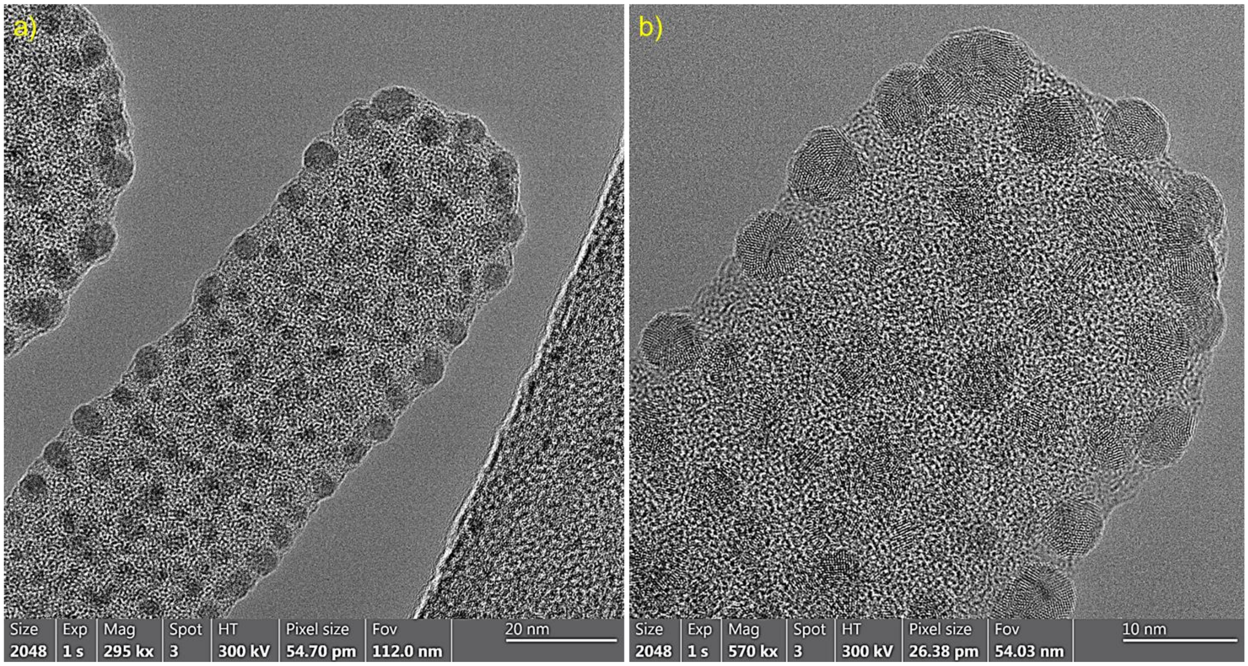

**Figure S9.** Low-resolution STEM micrographs of a rod-shaped Ag-CBT crystal under different magnification. The micrographs revealed the emergence of atom-resolved crystalline domains under electron beam irradiation.

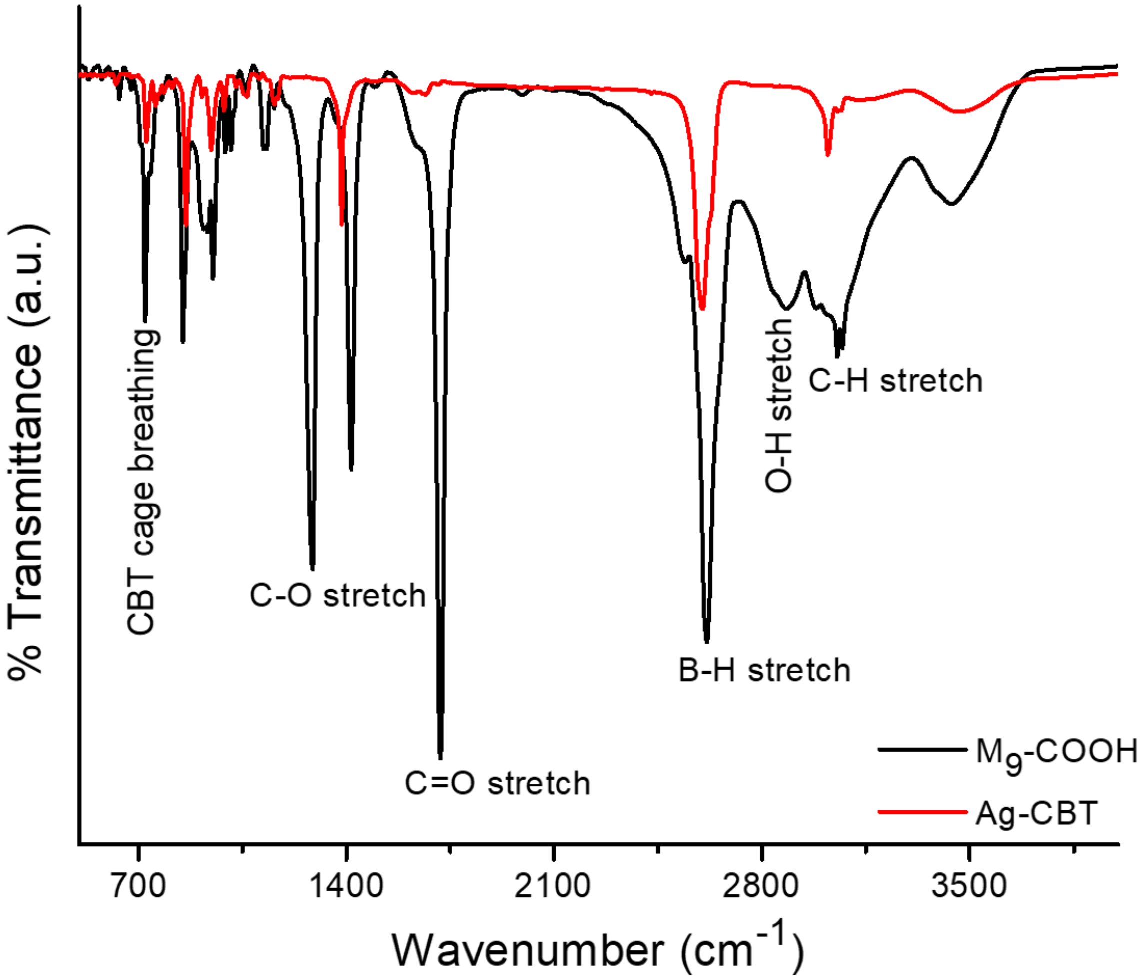

**Figure S10.** Comparative FT-IR spectra of $M_9$-COOH ligand and Ag-CBT framework solids. The decarboxylation of $M_9$-COOH in the Ag-CBT framework was evidenced by the disappearance of the 1717 $cm^{-1}$ (C=O stretching), 1286 $cm^{-1}$ (C-O stretching), and 2878 $cm^{-1}$ (O-H stretching) bands. The broad vibrational band observed at ~3500 $cm^{-1}$ is likely due to solvated water molecules.

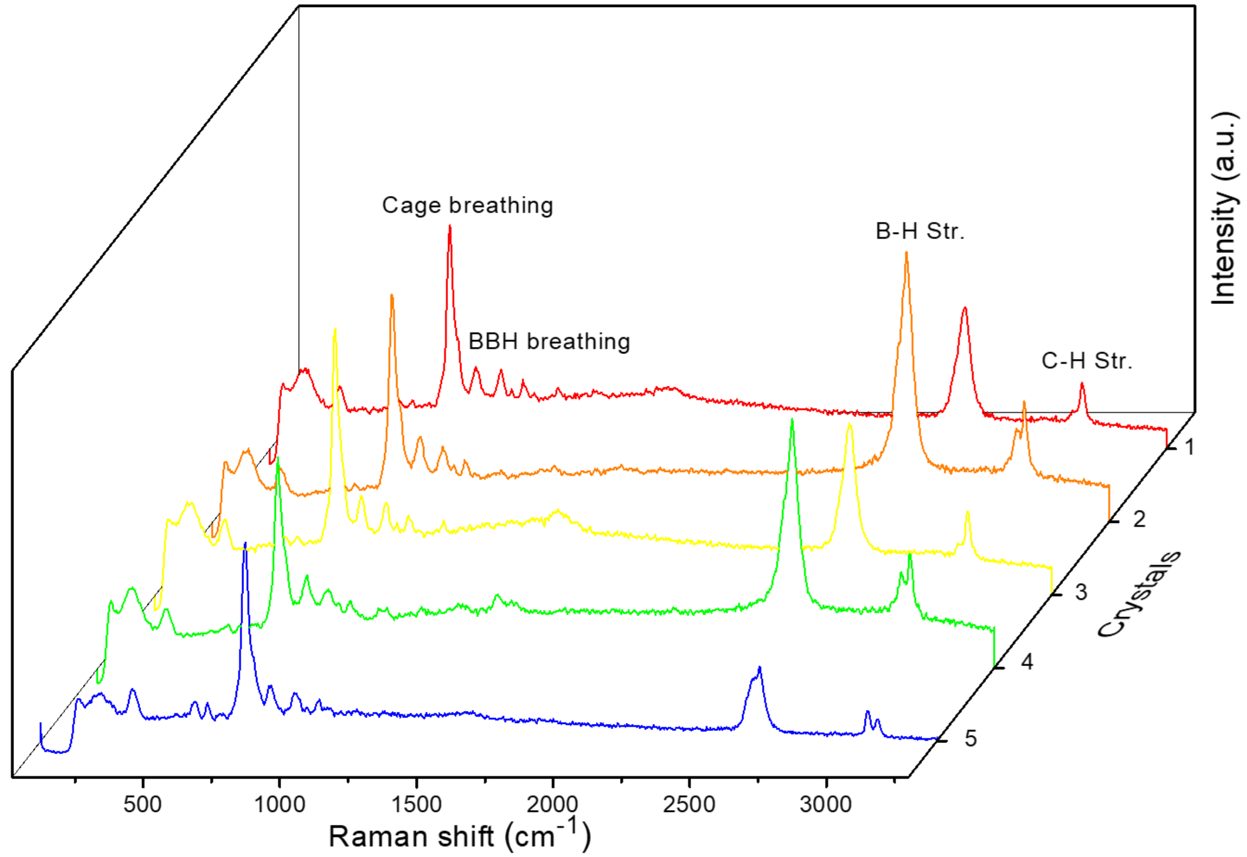

**Figure S11.** Raman spectroscopic data of Ag-CBT framework were collected, with each spectrum obtained from an individual crystal. The laser excitation used was 532 nm.

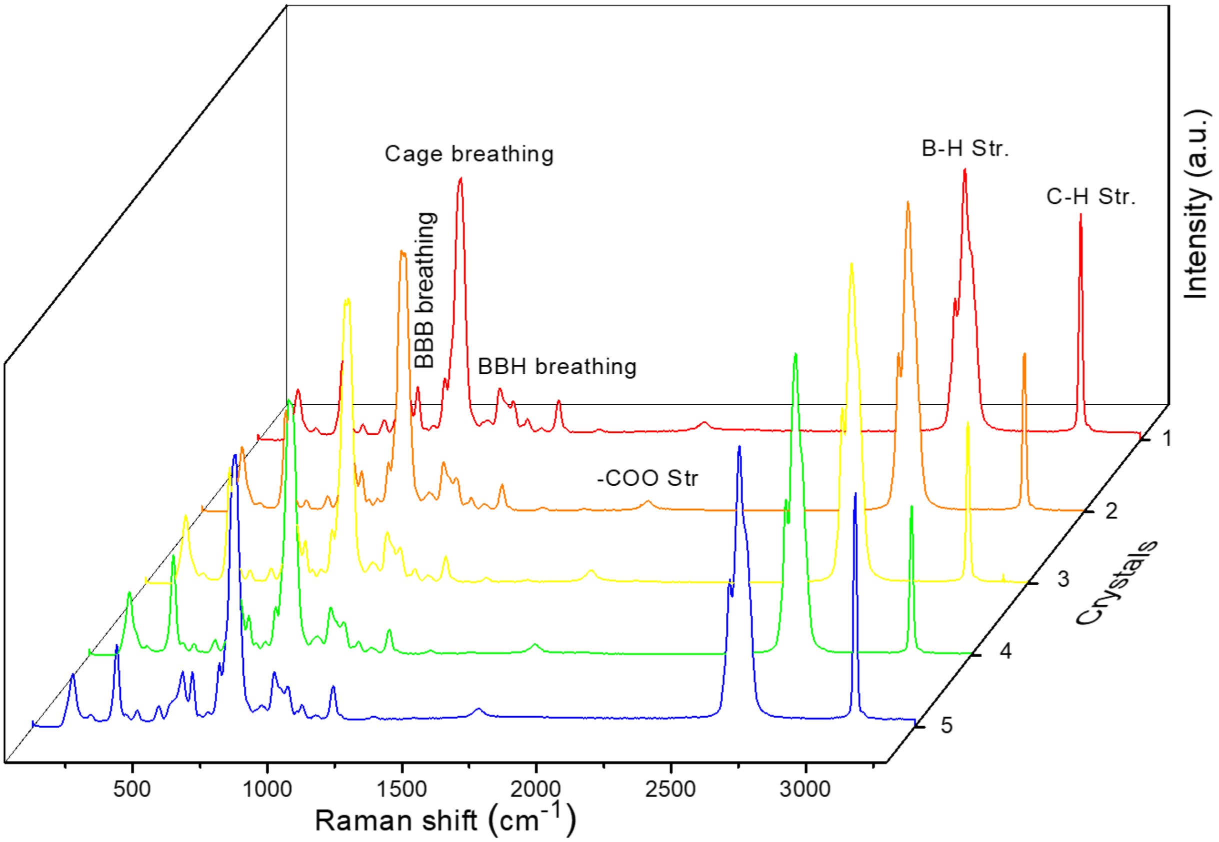

**Figure S12.** Raman spectroscopic data of M9-COOH ligand. Each spectrum was collected from an individual single crystal. The laser excitation used was 532 nm.

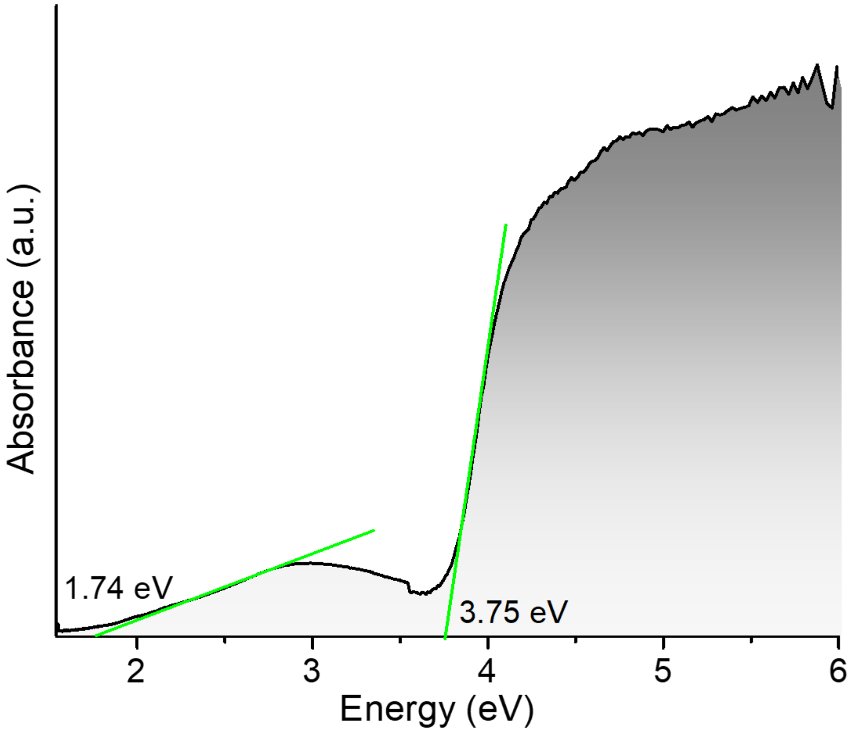

**Figure S13.** Solid-state UV-vis absorption spectrum of the Ag-CBT framework indicating two optical band gaps of 1.74 and 3.75 eV.

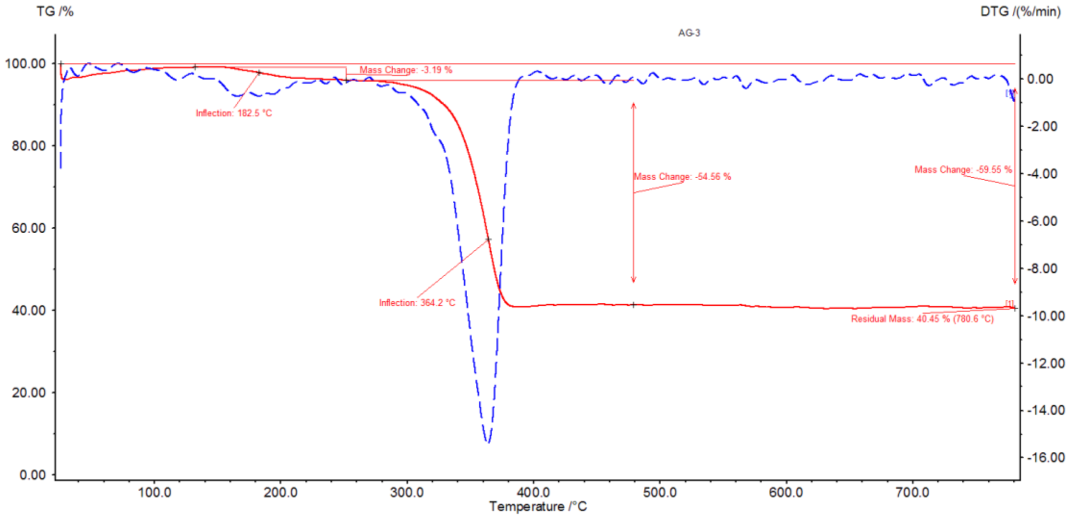

**Figure S14.** Thermogravimetric and differential thermal analysis plot of microcrystalline Ag-CBT chalcogenide framework. Minor variation (3.19 %) of the mass at 182.5 °C is due to the losses of adsorbed solvent molecules. The decomposition of the framework began at ~300 °C, with maximum mass loss observed at 364 °C.

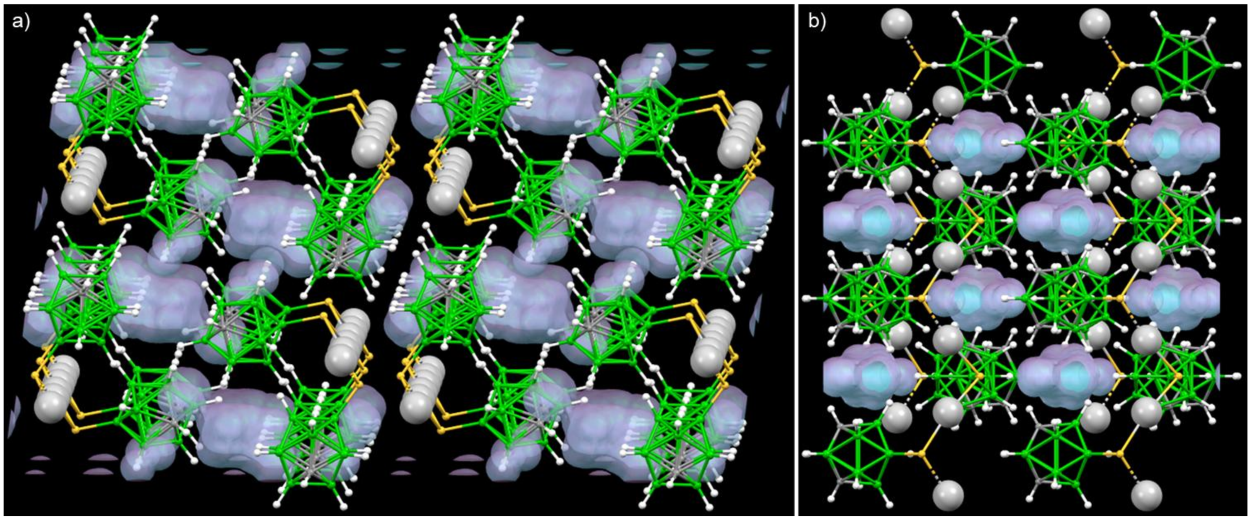

**Figure S15.** Void spaces present in the (2 × 2 × 2) lattices of the Ag-CBT chalcogenide framework. Voids are calculated using a grid spacing of 0.2 Å and radius of the probe as 0.75 Å. Such voids are present in the 6.5 % volume of the unit cell of the lattice.

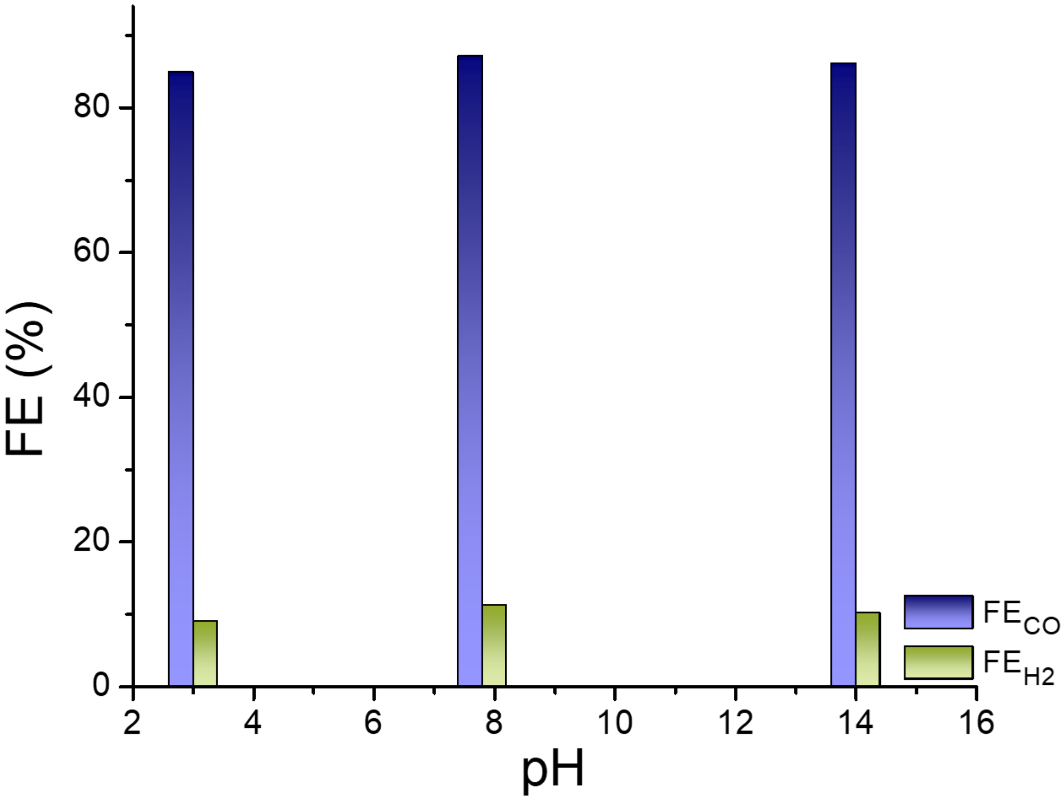

**Figure S16.** Variation in the Faradic efficiency of the Ag-CBT loaded electrode measured under three different pH conditions.

**Table S5.** Comparison between various silver based catalysts used for $CO_2$ electroreduction.

| Sl. No | Catalyst | Max $FE_{CO}$ (%) / Max $j_{CO}$ (mA $cm^{-2}$) | $E_0$ for $FE_{CO}$ (max) (V vs RHE) | Cell setup | Electrolyte | Reference |
|---|---|---|---|---|---|---|
| 1. | Ag foil | 70.5 | −0.75 | Two-compartment electrochemical cell | 0.5 M $KHCO_3$ | 7 |
| 2. | 3 nm Ag nanoparticles | 76.8 | −0.75 | Two-compartment electrochemical cell | 0.5 M $KHCO_3$ | 7 |
| 3. | 5 nm Ag nanoparticles | 84.4 | −0.75 | Two-compartment electrochemical cell | 0.5 M $KHCO_3$ | 7 |
| 4. | Ligand free Cubic Ag nanoparticle | 62.7/ 0.1 | -0.80 | H-cell | 0.5 M $KHCO_3$ | 8 |
| 5. | Ligand free octahedral Ag nanoparticle | 48.1/ 0.08 | -0.80 | H-cell | 0.5 M $KHCO_3$ | 8 |
| 6. | Nanoporous monolithic Ag nanoparticle | 92/ 30 | -0.70 | H-cell | 0.5 M $KHCO_3$ | 9 |

|  |  |  |  |  |  |  |
|---|---|---|---|---|---|---|
| 7. | Triangular Ag nanoplates | 96.8 | -0.746 | H-cell | 0.5 M $KHCO_3$ | 10 |
| 8. | Ag Nanocubes | 99 | -0.856 | Flow-cell | 0.1 M KHCO3 | 11 |
| 9. | $Ag_{25}$ cluster | 80/ 94 | -0.65 V | Flow shell | 1 M KOH | 12 |
| 10. | $ClAg_{14}$ (C≡C $^{t}Bu)_{12}$ Nanocluster | 80 /285 | -0.65 V | Flow shell | 0.5 M KOH | 12 |
| 11. | Ag-CBT chalcogenide framework solid | 86 /98 | -0.83 | Flow shell | 1 M KOH | This work |

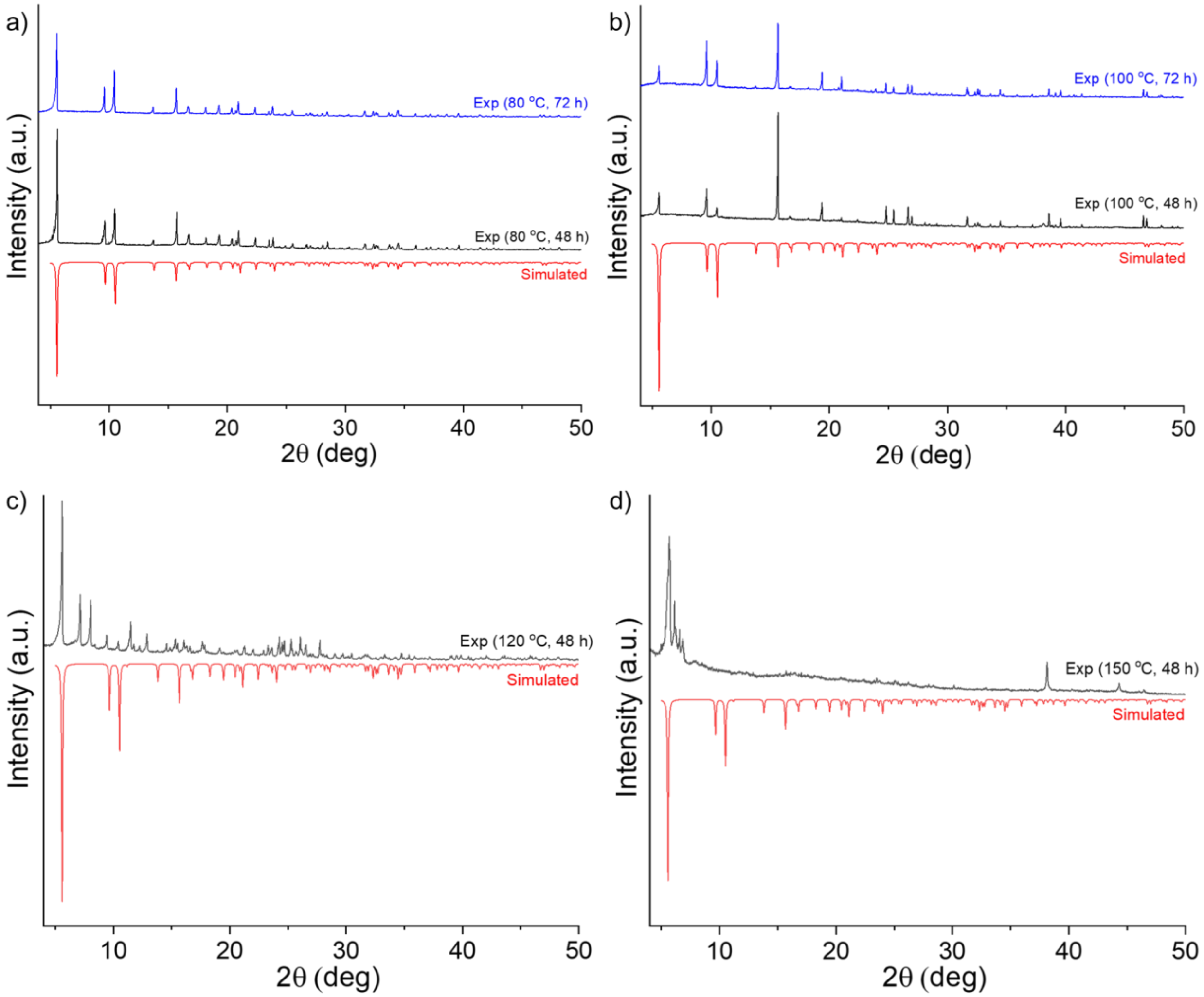

**Figure S17.** Comparison of simulated and experimental powder X-ray diffraction patterns for various synthetic products obtained from the solvothermal reaction of $AgNO_3$ and $M_9$-COOH at temperatures of a) 80 °C, b) 100 °C, c) 120 °C, and d) 150 °C.

**References:**

(1) Goronzy, D. P.; Staněk, J.; Avery, E.; Guo, H.; Bastl, Z.; Dušek, M.; Gallup, N. M.; Gün, S.; Kučeráková, M.; Levandowski, B. J.; Macháček, J.; Šícha, V.; Thomas, J. C.; Yavuz, A.; Houk, K. N.; Danlşman, M. F.; Mete, E.; Alexandrova, A. N.; Baše, T.; Weiss, P. S. Influence of Terminal Carboxyl Groups on the Structure and Reactivity of Functionalized M-Carboranethiolate Self-Assembled Monolayers. *Chem. Mater.* **2020**, *32* (15), 6800–6809.

(2) Liu, K.; Smith, W. A.; Burdyny, T. Introductory Guide to Assembling and Operating Gas Diffusion Electrodes for Electrochemical $CO_2$ Reduction. *ACS Energy Lett.* **2019**, *4* (3), 639–643.

(3) Kresse, G.; Hafner, J. Ab Initio Molecular-Dynamics Simulation of the Liquid-Metalamorphous- Semiconductor Transition in Germanium. *Phys. Rev. B* **1994**, *49* (20), 14251–14269.

(4) Perdew, J. P.; Chevary, J. A.; Vosko, S. H.; Jackson, K. A.; Pederson, M. R.; Singh, D. J.; Fiolhais, C. Atoms, Molecules, Solids, and Surfaces: Applications of the Generalized Gradient Approximation for Exchange and Correlation. *Phys. Rev. B* **1992**, *48* (11), 6673–6687.

(5) Kresse, G.; Joubert, D. From Ultrasoft Pseudopotentials to the Projector Augmented-Wave Method. *Phys. Rev. B - Condens. Matter Mater. Phys.* **1999**, *59* (3), 1758–1775.

(6) Nørskov, J. K.; Rossmeisl, J.; Logadottir, A.; Lindqvist, L.; Kitchin, J. R.; Bligaard, T.; Jónsson, H. Origin of the Overpotential for Oxygen Reduction at a Fuel-Cell Cathode. *J. Phys. Chem. B* **2004**, *108* (46), 17886–17892.

(7) Kim, C.; Jeon, H. S.; Eom, T.; Jee, M. S.; Kim, H.; Friend, C. M.; Min, B. K.; Hwang, Y. J. Achieving Selective and Efficient Electrocatalytic Activity for $CO_2$ Reduction Using Immobilized Silver Nanoparticles. *J. Am. Chem. Soc.* **2015**, *137* (43), 13844–13850.

(8) Yang, M.; Zhang, J.; Cao, Y.; Wu, M.; Qian, K.; Zhang, Z.; Liu, H.; Wang, J.; Chen, W.; Weixin, H. Facet Sensitivity of Capping Ligand-Free Ag Crystals in $CO_2$ Electrochemical Reduction to CO. *ChemCatChem* **2018**, *10*, 5128–5134.

(9) Lu, Q.; Rosen, J.; Zhou, Y.; Hutchings, G. S.; Kimmel, Y. C.; Chen, J. G.; Jiao, F. A Selective and Efficient Electrocatalyst for Carbon Dioxide Reduction. *Nat. Commun.*

**2014**, *5* (3242), 1–6.

(10) Liu, S.; Tao, H.; Zeng, L.; Liu, Q.; Xu, Z.; Liu, Q.; Luo, J. L. Shape-Dependent Electrocatalytic Reduction of $CO_2$ to CO on Triangular Silver Nanoplates. *J. Am. Chem. Soc.* **2017**, *139* (6), 2160–2163.

(11) Liu, S.; Sun, C.; Xiao, J.; Luo, J. L. Unraveling Structure Sensitivity in $CO_2$ Electroreduction to Near-Unity CO on Silver Nanocubes. *ACS Catal.* **2020**, *10* (5), 3158–3163.

(12) Seong, H.; Chang, K.; Sun, F.; Lee, S.; Han, S. M.; Kim, Y.; Choi, C. H.; Tang, Q.; Lee, D. $ClAg_{14}(C{\equiv}C^{t}Bu)_{12}$ Nanoclusters as Efficient and Selective Electrocatalysts Toward Industrially Relevant $CO_2$ Conversion. *Adv. Sci.* **2024**, *11* (2306089), 1–13.